# Singly-Resonant OPO for $CO_2$/$CH_4$ Dial Transmitter for Use in Atmospheric Studies

**Major Dr. Chat Chantjaroen**

*Department of Physics Academic Division, Chulachomklao Royal Military Academy*
*Corresponding Author. Email : chat539@hotmail.com*
*(Received: July 31, 2018; Revised: September 21, 2018; Accepted: October 2, 2018)*

**Abstract :** We report on a singly-resonant optical parametric oscillator (OPO) based on periodically poled MgO-doped $LiNbO_3$. The OPO was pumped by a Q-switch pulsed 1064-nm Nd:YAG laser and was seeded by an amplified 1571 nm DFB CW laser. The OPO is designed particularly for use as a aser source for a Differential Absorption Lidar (DIAL) for $CO_2$/$CH_4$ atmospheric concentration mapping. Maximum average output pulse energy of ~2 mJ and optical-to-optical conversion efficiency of up to ~20% have been achieved. Given the performance results of our frequency-agile OPO, we demonstrated a potential use of OPO in DIAL instruments for measurements of $CO_2$ (1571 nm) and CH4 (1645 nm).

**Keywords:** Nonlinear Optics, Parametric Process, Optical Parametric Oscillator, Optical Parametric Amplifier, Differential Absorption Lidar

## 1. Introduction

The atmospheric concentration of carbon dioxide ($CO_2$) increased over 40% from 278 parts per million (ppm) in 1750 to a present value of over 404 ppm [1] while the atmospheric concentration of methane (CH4) increased over 150% from 722 parts per billion (ppb) to over 1800 ppb over the same period [2]. The rate of increase of $CO_2$, averaged at 2.0 ppm/yr between 2002 and 2011, is the highest since direct $CO_2$ measurements began in 1958. In the fifth assessment report by the Intergovernmental Panel on Climate Change (IPCC) [3], the increases in $CO_2$ emissions from fossil fuel burning and land use are listed as the dominant causes for the observed increase in atmospheric $CO_2$ concentration. The changes in the atmospheric $CH_4$ concentration are less well understood. From 1980 until the late 1990's, the atmospheric $CH_4$ concentration grew from approximately 1570 ppb to 1760 ppb. From the late 1990's until about 2007, the atmospheric $CH_4$ concentration remained relatively constant. Beginning in 2007, the atmospheric $CH_4$ concentration began to increase again from 1760 ppb to the current 1803 ppb [2, 4, 5]. Anthropogenic emissions of $CH_4$

account for between 50% and 65% of total emissions with fossil emissions resulting from leaks in the fossil fuel industry infrastructure while natural leaks account for approximately 30% of total $CH_4$ emissions [3].

Recognizing the importance of these carbon-based molecules, an initial United States (U.S.) Carbon Cycle Science Plan was developed in 1999 [6] and has been updated in 2011 [7]. This updated U.S. Carbon Cycle Science Plan is aimed at organizing national research efforts to address three overarching questions including: 1. How do natural processes and human actions affect the carbon cycle, 2. How do policy and management decisions affect the level of primary carbon containing gases $CO_2$ and $CH_4$ in the atmosphere, and 3. How are ecosystems, species, and natural resources impacted by increasing greenhouse gases. This U.S. Carbon Cycle Science Plan, along with two reports from the National Research Council [8, 9], recognize the need to develop remote sensing tools capable of both $CO_2$ and $CH_4$ observations from ground, aircraft, and space-based platforms as important observational tools for carbon cycle science.

Differential absorption lidar (DIAL) is an active remote sensing technique that has the potential for spatially mapping $CO_2$ and $CH_4$ that can address the need for remote sensing tools stated by the U.S. Carbon Cycle Science Plan and the National Research Council. The DIAL technique utilizes two closely spaced laser transmitter wavelengths, one centered on the molecular absorption feature of interest, referred to as the on-line wavelength, and the second far removed from the absorption feature and referred to as the off-line wavelength. The difference between the scattered light at the on-line and off-line wavelengths can be used to retrieve the range information of the number density of the molecular species of interest [10]. The DIAL technique is an active remote sensing technique and offers several advantages over passive measurement techniques including high spatial resolution, high measurement specificity with minimal interference from other atmospheric constituents, lack of the need for external lighting, and relatively simple inversion methods for retrieval of number density profiles compared to passive sensor retrievals.

Research efforts to develop remote sensing instrumentation to meet the challenging accuracy and precision for $CO_2$ observations of better than 1% needed for carbon cycle studies [11] require leading researchers to consider many different instrument architectures. Instruments being developed for airborne deployment and future satellite deployment are utilizing an integrated path differential absorption (IPDA) measurement technique that provides a column averaged $CO_2$ number density [12, 13]. These instruments operate at either 1.57 μm or 2.0 μm and provide coarse range measurements by using several wavelengths across the absorption spectra and the pressure dependence of the absorption linewidth to retrieve profiles. Ground based instruments also employ the IPDA technique at both the 1.57 μm and 2.0 μm wavelengths. While

these instruments can provide the accuracy needed for carbon cycle science, they typically provide a column averaged $CO_2$ value and do not speak to the spatial distribution of the $CO_2$. Initial work on pulsed DIAL instruments for ground-based $CO_2$ observations has been discussed in the literature with a handful of DIAL instruments demonstrating $CO_2$ profile retrievals [14-22]. Uchiumi et al. [14] developed a DIAL instrument that utilized a Ti:Sapphire laser to pump a Raman cell. Utilizing the second Stoke's line, the transmitter was able to produce an output wavelength raging between 1.6 μm and 2.3 μm. $CO_2$ measurements between 300 m and 700 m range were obtained with approximately a ±70 ppm error at 700 m. Kock et al. [15] describe a DIAL instrument based on a Ho:Tm:YLF laser operating at 2.05 μm. A single $CO_2$ concentration measurement was retrieved over 1200 m with an error of 9.9 ppm. Sakaizawa et al. [16] demonstrated a DIAL instrument for profiling atmospheric $CO_2$ based on an Nd:YAG pumped optical parametric oscillator (OPO). This instrument was able to measure $CO_2$ profiles to 5.2 km with a 5-hour integration time. Reported errors were less than 2%. Nagasawa et al. [17] demonstrated a DIAL instrument based on an Nd:YAG pumped optical parametric generator (OPG) combined with an optical parametric amplifier (OPA) laser transmitter. Daytime vertical profiles were made to 6 km with a 3-km range bin with errors of approximately 5 ppm. Johnson et al. [18] most recently reported on a DIAL instrument for carbon sequestration site monitoring based on an injection seeded fiber amplifier. Horizontal profiles out to 2.5 km were obtained with a 50 ppm error. While these instruments have demonstrated $CO_2$ profiling ability, they do not meet the needed measurement accuracy for carbon cycle studies, require long integration times, and typically have a low range resolution.

Research efforts to develop remote sensing tools for $CH_4$ monitoring are in their infancy. A methane DIAL developed by Ikuta et al. [23] utilized a Nd:YAG laser to pump a Ti:Sapphire laser. The output from the Ti:Sapphire laser was then shifted to 1.67 μm using the nonlinear Raman scattering technique. This DIAL can detect 6000 ppm at 130 m, well above the needed sensitivity for atmospheric measurements. More recent work by Fix et al. [12] has demonstrated a potential laser source for CO2 and $CH_4$ DIAL instruments. This laser utilizes a Nd:YAG pumped, injection seeded OPO in combination with an OPA. Shuman et al. [24] describe the development of a second laser source as another potential transmitter for CH4 instruments based on a Nd:YAG pumped OPO. While work is underway to develop DIAL instruments for methane profiling, no DIAL instrument is currently operating routinely with the needed sensitivity.

Refaat et al. [25] have modeled the performance of DIAL instruments for monitoring $CO_2$ at 1571 nm and $CH_4$ at 1645 nm and conclude that 3 mJ pulses at a 1 kHz pulse repetition rate would allow atmospheric $CO_2$ and $CH_4$ measurements to be made beyond 3 km

(4 km) with a 5-minute averaging time with an error of less than 0.5% (1%). Research efforts leading to new laser sources capable of meeting the requirements set out by Refaat et al. [22] are needed for DIAL instruments to be capable of monitoring $CO_2$ and $CH_4$ with the required sensitivity to meet the remote sensing capability as stated by both the U.S. Carbon Cycle Science Plan and the National Research Council.

In this paper, a DIAL laser transmitter design capable of operating at both 1571 nm and 1645 nm is presented. Our initial design, operating at 1571 nm, uses a singly-resonant optical parametric oscillator (OPO) pumped by a Q-switch pulsed 1064 nm Nd:YAG laser and seeded by an amplified 1571 nm DFB CW laser. The OPO uses a linear cavity with a periodically poled lithium niobate crystal (PPLN) as a nonlinear gain material inside. The measured performance of the singly resonant OPO laser is compared with the SNLO model providing a prediction for further improvement in the laser transmitter design.

This paper is organized as follows. The experimental setup is described in section 2. Results from the laser performance are discussed in section 3. Finally, some brief concluding comments are presented in section 4.

## 2. Experimental setup

*2.1 OPO system*

A schematic of the OPO is shown in Fig. 1. A Big Sky Laser Ultra series flash-lamp-pumped Q-switch Nd:YAG laser of 1064 nm wavelength with 10-ns pulse duration and 20 Hz pulse repetition frequency (PRF) was used as a pump laser. A Q-photonics distributed feedback (DFB) continuous wave (CW) laser of 1571 nm wavelength with 10 mW maximum power was used as a seed laser. The IPG Photonics fiber amplifier was used to amplify the seed power to about 160 mW. By applying a half-wave-plate and a Glan polarizer on both lasers, we could adjust the pump energy and seed power without changing their Gaussian beam properties and thus making the system alignment consistent. To maximize the system efficiency, the pump and seed beams were fully overlapped and focused at the same spot within the crystal. In addition to the design, another half-wave-plate was installed before the focusing lens in each beam path to increase the efficiency by allowing us to rotate and match the polarization direction of the beam to the optical axis of the crystal. The nonlinear crystal was a periodically poled lithium niobate (PPLN) crystal with a 5% magnesium-oxide doped (Mg:LiNbO3) by AdvR. The crystal was placed in a custom-built aluminum heater for temperature control needed for adjusting the output wavelengths in the quasi-phase-matching process. The linear cavity used in the OPO consisted of two mirrors—one flat and one concave with 500 mm radius of curvature. The flat mirror has a measured reflectivity of 99% at the seed wavelength (1571 nm) and 24% at the pump wavelength (1064 nm). The curved mirror has a measured reflectivity of 48% at the seed and 21% at the pump wavelength. The reflectivity at the idler wavelength (3297 nm) is

estimated to be 30% for both mirrors. The cavity length was 492 mm with the flat mirror located near the entrance face of the crystal.

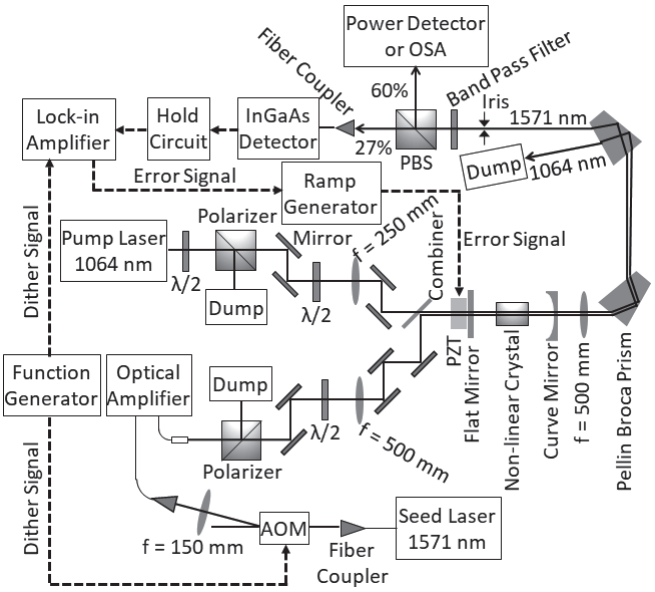


**Fig. 1.** Schematic of the OPO with the locking system. For OPG and OPA, the locking system and the optical cavity are excluded, and the seed laser is bypassing the AOM and is fiber coupled directly into the optical amplifier. The seed laser is turned on for OPA and turned off for OPG.

As shown in Fig. 1, the flat mirror was mounted on a piezo-electric transducer (PZT) which was used to mechanically adjust the cavity length relevant to the signal received by the locking system. The locking system used a dither locking technique to adjust the cavity length that could maintain the cavity at resonance. The locking system was consisted of a function generator (Stanford Research Systems DS345) and an acousto-optic modulator (AOM) (Isomet 1205C-2 modulator with 620C-80 driver) to modulate the seed laser. This modulated signal was then amplified and incident on the optical cavity. An InGaAs detector (New Focus 2011) was used to detect the cavity transmission output and convert the signal into an analog signal. A hold circuit was used to clean unwanted parts of this output signal before it was sent to the lock-in amplifier (Stanford Research Systems SR510). A ramp generator (Burleigh RC-44) was used to control a piezo-electric transducer (PZT) in accordance with the error signal sent from the log-in amplifier. Through contractions and expansions of the PZT in which the flat mirror is mounted, the cavity length can be adjusted to maintain the resonance. Two Pellin-Broca prisms were used to separate the output beam by wavelengths. The third focusing lens was designed to focus the output beam near the detector location, otherwise the highly-divergent beam was impossible to detect by the detector. An energy meter (Thorlabs model PM100D with an ES111C power detector) was used for the measurement of output energy. An optical spectrum analyzer (OSA) (Agilent model 86142B) was used for the measurement of output spectra. For measurement accuracy, the detector and OSA were blocked from wavelengths other than 1571 nm by surrounding them with a black box (not shown in the diagram) which had an entrance only through the iris and the band pass filter.

*2.2 PPLN crystal analysis*

Four PPLN crystals with poling periods of 30.860, 31.153, 31.250, and 31.546 μm were characterized in this project. To select a proper crystal that will produce the output signal wavelength near 1571 nm needed for $CO_2$ measurements, each crystal of different sizes was placed in a custom-built aluminum heater which was heated by a TEC and monitored by a thermal sensor. The crystal temperature scanning used the OPG setup and the output signal wavelength was measured by the OSA.

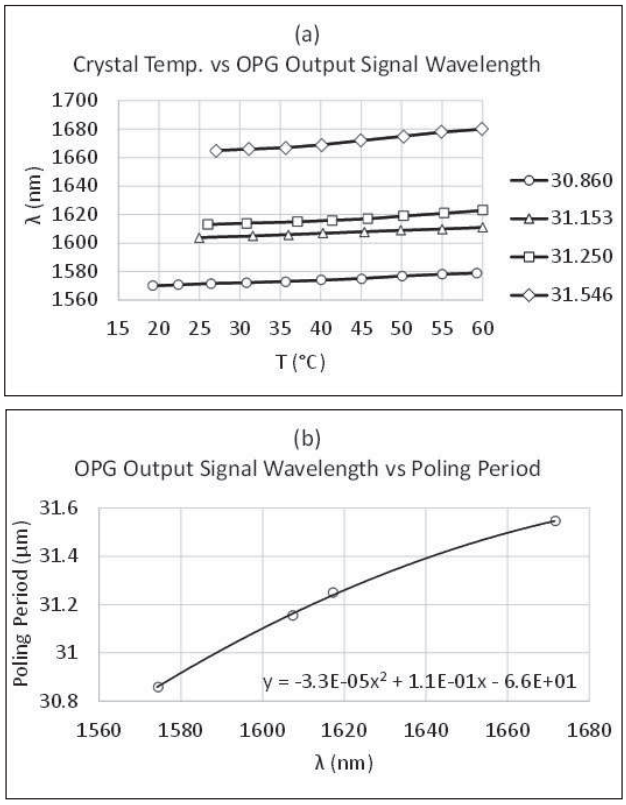


**Fig. 2.** (a) Temperature/wavelength tuning characteristics of the PPLN crystals with different poling periods (30.860, 31.153, 31.250, and 31.546 μm) in a 1064 nm pumped OPG setup. (b) Quadratic trend of the PPLN crystal poling period with respect to the average OPG output signal wavelength plotted in (a).

As shown in the temperature scanning results in Fig. 2(a), the 30.860-μm poling period crystal was selected to be used in the experiment since it could produce the output signal wavelength near 1571 nm needed for $CO_2$ measurements. The trend on how the output signal wavelength increases with respect to the poling periods of these crystals shown in Fig. 2(b) is used to estimate a poling period of 31.427 μm needed for $CH_4$ measurements near 1645 nm wavelength.

## 3. Results

*3.1 Output spectra*

OPG/OPA output spectra shown in Fig. 3 can be used to demonstrate how well the system is aligned by looking at two forms of overlaps—spectral overlap and spatial overlap. Spectral overlap is the overlap between the wavelengths of the spontaneous emission of the crystal and the seed laser. This may be evaluated by looking at the OPG output spectrum and the seed spectrum. Fig. 3(a) demonstrates a case of poor spectral overlap since the peak of OPG spectrum does not line up with the peak of the seed spectrum, while Fig. 3(b) and 3(c) demonstrate a case of good spectral overlap since the peak of the OPG spectrum lines up well with the peak of the seed spectrum. Spatial overlap is the overlap between the pump and seed beams within the crystal. This may be evaluated by comparing the features of the OPG and OPA output spectra. As shown in Fig. 3(b), the sidebands of the OPA spectrum, which is nearly as broad as the OPG spectrum, indicates a poor spatial overlap. Ideally a good spatial overlap should provide OPA sidebands that are narrower than the OPG spectrum as shown in Fig. 3(c).

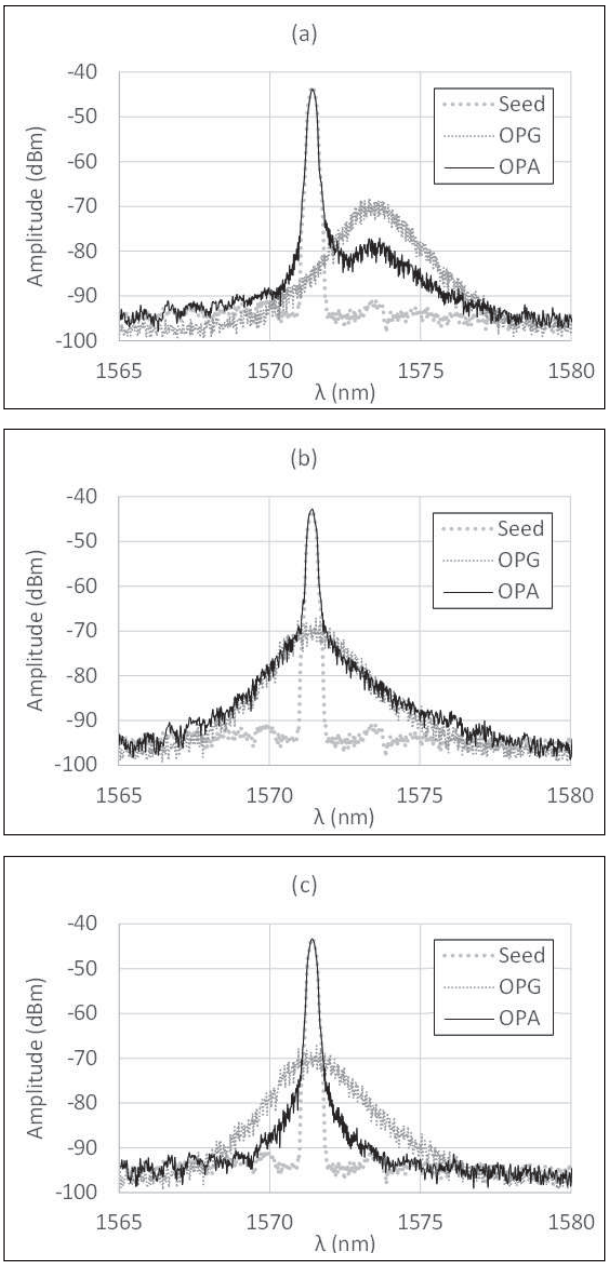


**Fig. 3.** Output spectra. (a) Demonstration of poor spectral overlap case. Notice how the peak of the OPG spectrum does not line up with the peak of the seed laser spectrum. (b) Demonstration of poor spatial overlap case. When the seed beam is not collinear with the pump beam, the output OPA spectrum becomes very broad at the bottom which could be as broad as the OPG. However, the system has good spectral alignment since the peak of the OPG line up with the peak of the seed laser. (c) Demonstration of both good spectral and spatial overlap case. The peak of the OPG spectrum coincides with the peak of the seed laser spectrum and the sidebands of the OPA spectrum are much narrower than those of the OPG.

The broadening of the OPA sidebands in the case of poor spatial overlap is most likely the result of domination of the spontaneous emission over the stimulated emission when the seed beam is not collinear with the pump beam. It should be noted that the spectrum measurements shown in Fig. 3 cannot be used for comparison between the output intensities of OPG/OPA and the seed. It appears in these plots that the seed intensity is almost as high as the OPA intensity which is not the case. This is because the OSA captures and handles the OPG/OPA outputs, which are pulsed and the seed laser, which is CW, differently. For this reason, separate output energy measurements using a different instrument were performed to make the energy comparisons.

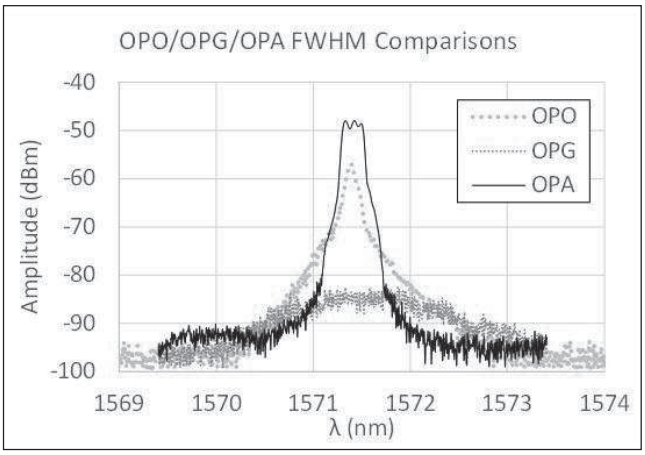


**Fig. 4.** FWHM comparisons between OPG, OPA, and OPO. For each plot, FWHM is the width of the feature measured at the amplitude of -3 dBm down from the peak.

Full width at half maximum (FWHM) for the OPG/OPA/OPO was measured from Fig. 4. In the plots, the OSA was set at the highest resolution of 0.06 nm with a high sensitivity of -90 dBm. Data in each plot are averaged between 5 to 10 pulses or until the pattern of the plot does not appear to change. In an amplitude unit of dBm, FWHM is measured at -3 dBm down from the peak of the spectrum. From the figure, the FWHM of the OPG, OPA, and OPO were measured to be 1.400, 0.2232, and 0.0941 nm, respectively. This makes the OPO the best option for a DIAL laser transmitter which requires a narrow linewidth.

It should be noted that the spectrum measurements by the OSA in Fig. 4 cannot be used for intensity comparison between the OPG/OPA and OPO. Although the OPO is built upon the OPA setup, adding an optical cavity will change the output beam shape and direction. Even with our best realignment efforts, the amount of output beam that is fiber coupled into the OSA still reduces significantly. Consequently, the OPO peak appears smaller than the OPA peak, but this does not necessarily mean the OPA output energy is greater than that of the OPO. To compare output energies between the OPA and OPO, energy measurements were conducted separately. Nevertheless, FWHM determined from the OSA measurements can be used for comparison among OPG, OPA, and OPO.

*3.2 Output energy*

Results of the output energy measurements using a Thorlabs energy meter model PM100D with ES111C power detector are shown in Fig. 5. The plot in Fig. 5(a) is the output at the crystal exit location in which output measurements at the detector location have been corrected by the transmissions of all the optical elements along the path shown in Fig. 1. The optical-to-optical conversion efficiency shown in Fig. 5(b) is defined as a percentage ratio between the output signal energy and the input pump energy. At below 8 mJ input pump energies, the output energy and conversion efficiency from the OPO is the highest, which was expected. However, at above 8 mJ input pump energies, the OPO output energies drop down and become lower than that of OPG and OPA. This is likely due to the phase mismatch resulting from the increase of crystal temperature at higher input pump energies. The conversion efficiency reaches a maximum of about 18%, 19%, and 20% for OPG, OPA, and OPO, respectively. It should be noted that all experimental measurements are limited at 12 mJ input pump

energy to prevent damaging the crystal and all other optics.

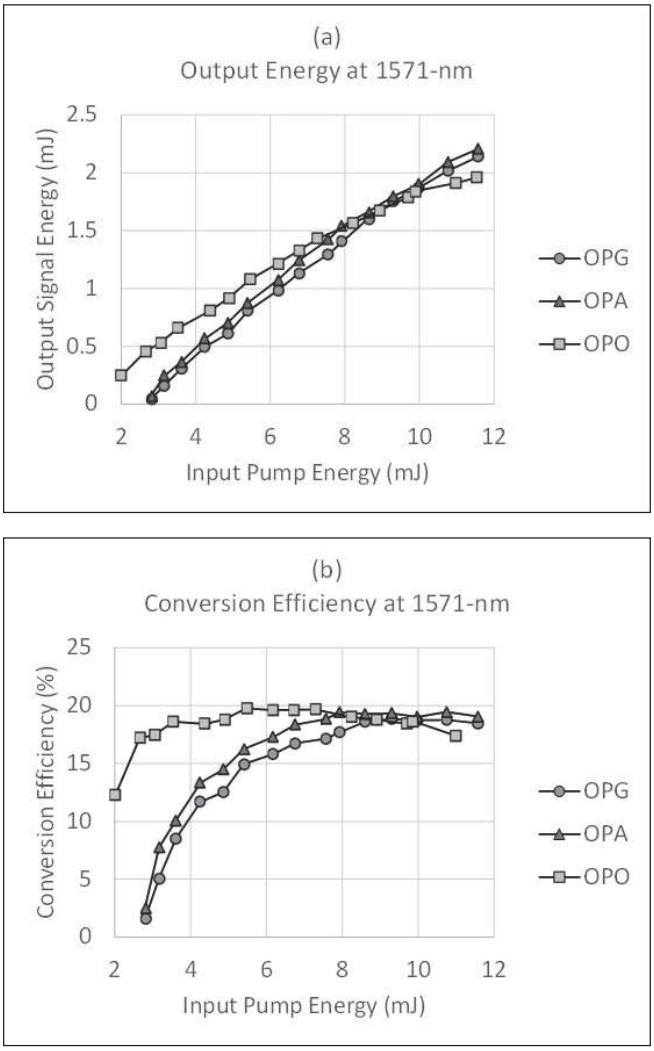


**Fig. 5.** (a) Output signal energy at 1571.406 nm wavelength of the OPG, OPA, and OPO. (b) The corresponding optical-to-optical conversion efficiency of OPG, OPA, and OPO.

*3.3 SNLO comparison*

To estimate the values of the effective nonlinear coefficient, deff, which acts as a gain term and the quasi phase mismatch factor, Δk, which acts as a loss term in the system, the OPA experimental data is compared with the theoretical OPA model in SNLO developed at Sandia National Laboratory [26]. In the comparisons, all SNLO input parameters are entered based on our actual experimental setup. By varying the input values of the pump energy, $d_{eff}$ and Δk, SNLO can calculate and predict the output signal energy of the system. The conversion efficiencies are calculated based on the output signal energy acquired from SNLO and plotted with the experimental data as shown in Fig. 6(a) for comparison. The best-fit result to the experimental data has $d_{eff} \approx 13$ pm/V and $\Delta k \approx 300\ m^{-1}$ as shown by the red curve in the plot. It should be noted that, in the comparison, the experimental data at low input pump energies of below 3 mJ and at high input pump energies of above 7 mJ were neglected. The reason for neglecting the low pump energies is that the detector cannot accurately detect extremely low output energies and thus produces large errors. The reason for neglecting the high pump energies is because SNLO model does not take into account the effect of crystal saturation at high pump energies.

The estimated value of deff from SNLO OPA model was used along with other actual experiment parameters as SNLO OPO model inputs. It should be noted that the SNLO OPO model assumes a symmetric cavity. Therefore, the inputs for the flat mirror are modified as if they are for another curved mirror that would make the cavity symmetric. For SNLO OPO model, Δk is set to zero for the case of perfect

quasi-phase-matching. Results from the SNLO model in comparison with the OPO measurements are shown in Fig. 6(b) and 6(c). Although with a lot of noise, the theoretical prediction in SNLO and the experimental data show good agreement.

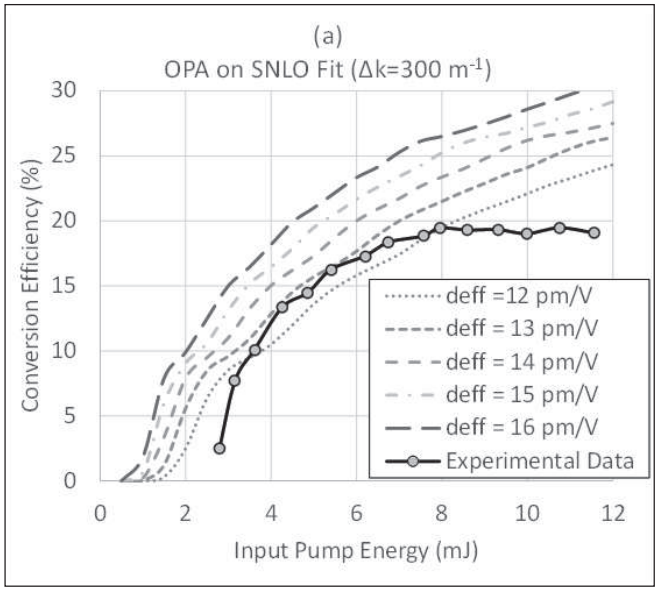


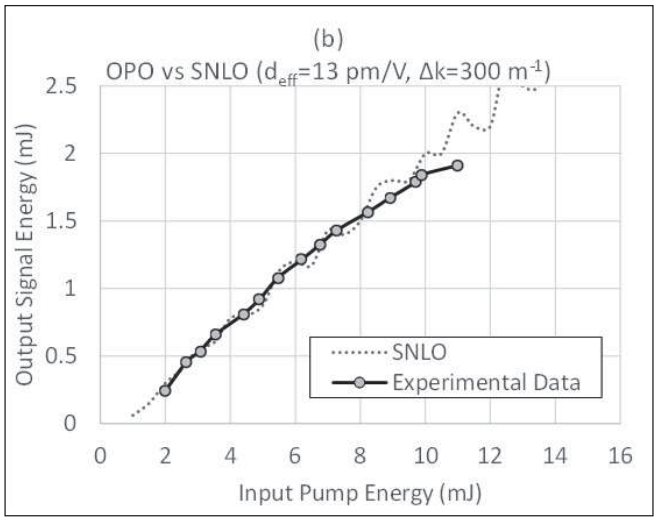


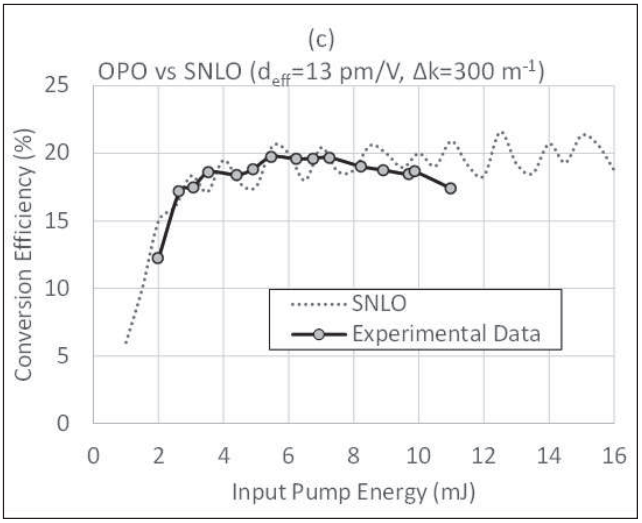


**Fig. 6.** (a) OPA conversion efficiency comparison between the experimental data and SNLO model. (b) OPO output signal energy comparison between the experimental data and SNLO model. (c) OPO conversion efficiency comparison between the experimental data and SNLO mode.

## 4. Conclusion

The goal of our development of the near-infrared OPO is to be used in the application of atmospheric studies by implementing it in a DIAL laser transmitter for the spatial mapping of $CO_2$ and $CH_4$ concentrations. We presented the first phase results of a singly-resonate OPO using a PPLN crystal in a linear cavity with a dither locking technique. The OPO was pumped with a Q-switch 1064 nm Nd:YAG laser and seeded with a 1571 nm DFB CW laser. We obtained an output signal at the on-line wavelength for a $CO_2$ DIAL of 1571.406 nm with a narrow linewidth of 0.0941 nm FWHM and 2 mJ averaged pulsed energy. The optical-to-optical conversion efficiency reached

about 20%. Good agreement between the theoretical prediction in SNLO and the experimental data confirms experimental success of the OPO. Further improvements of the OPO design based on the SNLO modeling could potentially meet the requirement of the DIAL transmitter.

## 5. Acknowledgement

I would like to thank Chulachomklao Royal Military Academy for providing financial support and opportunity to conduct this research. I would also like to thank Dr. Kevin Repasky and Montana State University for providing opportunity, facility, grant, and supports in many aspects.

## 6. References

(1) E. Dlugokenchy and P Tans, 2017. NOAA/ESRL http://www.esrl.noaa.gov/gmd/ccgg/trends.

(2) National Oceanic and Atmospheric Administration, 2017. NOAA/ESRL http://www.esrl.noaa.gov/gmd/aggi.

(3) P. Ciais, C. Sabine, G. Bala, L. Bopp, V. Brovkin, J. Canadell, A. Chhabra, R. DeFries, J. Galloway, M. Heimann, C. Jones, C. Le Quere, R.B. Myneni, S. Piao, and P. Thornton, 2013. Carbon and Other Biogeochemical Cycles. In: Climate Change 2013: The Physical Science Basis. Contribution of Working Group I to the Fifth Assessment Report of the Intergovernmental Panel on Climate Change (Stocker, T.F., D. Qin, G.-K. Plattner, M. Tignor, S.K. Allen, J. Boschung, A. Nauels, Y. Xia, V. Bex and P.M. Midgley (eds.)). Cambridge, United Kingdom and New York, NY, USA : Cambridge University Press.

(4) E. J. Dlugokencky, L. Bruhwiler, J. W. C. White, L. K. Emmons, P. C. Novelli, S. A. Montzka, K. A. Masarie, P. M. Lang, A. M. Crotwell, J. B. Miller, and L. V. Gatti, 2009. Observational constraints on recent increases in the atmospheric CH4 burden. Geophys. Res. Lett, 36.

(5) R.M. Measures and G. Pilon, 1972. A study of tunable laser techniques for remote mapping of specific gaseous constituents of the atmosphere. Opt. Quant. Electron, 4(2) : 141-153.

(6) J. L. Sarmiento, J. Louis, and C. W. Steven, 1999. A U.S. carbon cycle science plan. Boulder, CO, USA : University Corporation for Atmospheric Research.

(7) A. M. Michalak, B. J. Robert, M. Gregg, L. S. Christopher, and the Cabon Cycle Science Working Group, 2011. A U.S. Carbon Cycle Science Plan. Boulder, CO, USA : University Corporation for Atmospheric Research.

(8) National Research Council, 2007. Earth Science and Applications from Space: National Imperatives for the Next Generation and Beyond. USA : The National Academy Press.

(9) National Research Council, 2010. Verifying Greenhouse Gas Emissions: Methods to Support International Climate Agreements. USA : The National Academy Press.

(10) L. S. Rothman, A. Barbe, D. C. Benner, L. R. Brown, C. Camy-Peyret, M. R. Carleer, K. Chance, C. Clerbaux, V. Dana, V. M. Devi, A. Fayt, J. M. Flaud, R. R. Gamache, A. Goldman, D. Jacquemart, K. W. Jucks, W. J. Lafferty, J. Y. Mandin, S. T. Massie, V. Nemtchinov, D. A. Newnham, A. Perrin, C. P. Rinsland, J. Schroeder, K. M. Smith, M. A. H. Smith, K. Tang, R. A. Toth, J. Vander Auwera, P. Varanasi, and K. Yoshino, 2003. The HITRAN molecular spectroscopic database. J. Quant. Spectrosc. Radiat. Transfer, 82 : 5–44.

(11) P. J. Rayner and D. M. O'Brien, 2001. The utility of remotely sensed CO2 concentration data in surface source inversions. Geophys. Res. Lett., 28 : 175.

(12) A. Fix, C. Budenbender, M. Wirth, M. Quatrevalet, A. Amediek, C. Kiemle, and G. Ehret, 2011. Optical Parametric Oscillators and Amplifiers for Airborne and Spaceborne Active Remote Sensing of $CO_2$ and $CH_4$. Pro. SPIE, 8182 : 818206.

(13) J. B. Abshire, H. Riris, C. J. Weaver, J. Moa, G. R. Allan, W. E. Hasselbrack, and E. V. Browell, 2013. Airborne measurements of CO2 column absorption and range using a pulsed direct detection integrated path differential absorption lidar. Appl. Opt., 52 : 4446.

(14) M. Uchiumi, N. J. Vasa, M. Fujiwara, S. Yokoyama, M. Maeda, and O. Uchino, 2003. Development of DIAL for CO2 and CH4 in the atmosphere. Pro. SPIE, 4893 : 141.

(15) G. J. Koch, B. W. Barnes, M. Petros, J. Y. Beyon, F. Amzajerdian, J. Yu, R. E. Davis, S. Ismail, S. Vay, M. J. Kavaya, and U. Singh, 2004. Coherent differential absorption lidar measurements of $CO_2$. Appl. Opt., 43 : 5092.

(16) D. Sakaizawa, C. Nagasawa, T. Nagai, M. Abo, Y. Shibata, M. Nakazato, and T. Sakai, 2009. Development of a 1.6 μm differential absorption lidar with quasi-phase matching optical parametric oscillator and photon counting detector for the vertical $CO_2$ profile. Appl. Opt., 48 : 748.

(17) C. Nagasawa, M. Abo, Y. Shibata, T. Nagai, and M. Tsukamoto, 2011. Direct detection 1.6 μm DIAL for measurements of $CO_2$ concentration profiles in the troposphere. Pro. SPIE, 8182 : 81820G.

(18) W. Johnson, K. S. Repasky, and J. L. Carlsten, 2013. Micropulse differential absorption lidar for identification of carbon sequestration site leakage. Appl. Opt., 52 : 2994.

(19) F. Gibert, P. H. Flamant, D. Bruneau, and C. Loth, 2006. Two micrometer heterodyne differential absorption lidar measurements of the atmospheric $CO_2$ mixing ratio in the boundary layer. Appl. Opt., 45 : 4448.

(20) A. Amediek, A. Fix, M. Wirth, and G. Ehret, 2008. Development of an OPO system at 1.57 μm for integrated path DIAL measurements of atmospheric carbon dioxide. Appl. Phys. B, 92 : 295.

(21) S. Kameyama, M. Imaki, . Hirano, S. Ueno, S. Kawakami, D. Sakaizawa, and M. Nakajima, 2009. Development of a 1.6 ตm continuous wave modulation hard target differential absorption lidar system for $CO_2$ sensing. Opt. Lett., 34 : 1513.

(22) T. F. Refaat, S. Ismail, G. J. Koch, M. Rubio, T. L. Mack, A. Notari, J. E. Collins, J. Lewis, R. De Young, Y. Choi, M. N. Abedin, and U. N. Singh, 2011. Backscatter 2 μm Lidar Validation for Atmospheric $CO_2$ Differential Absorption Lidar Applications. IEEE Transactions on Geosciences and Remote, 49 : 572.

(23) K. Ikuta, N. Yoshikane, N. Vasa, Y. Oki, M. Maeda, M. Uchiumi, Y. Tsumura, J. Nakagawa, and N. Kawada, 1999. Differential Absorption Lidar at 1.67 μm for remote sensing of Methane Leakage. Japanese J. Appl. Phys., 38 : 110.

(24) T. Shuman, R. Burnham, A. R. Nehrir, S. Ismail, J. W. Hair, T. Refaat, 2013. Efficient 1.6 Micron Laser Source for Methane DIAL. Pro. SPIE, 8872 : 88720A.

(25) T. F. Refaat, S. Ismail, A. R. Nehrir, J. W. Hair, J. H. Crawford, I. Leifer, and T. Shuman, 2013. Performance evaluation of a 1.6 μm methane DIAL system from ground, aircraft and UAV platforms. Opt. Express, 21 : 30415-30432.

(26) AS-Photonics, 2017. SNLO. http://www.as-photonics.com/snlo.